Supercell Thunderstorms in Complex Topography—How Mountain Valleys with Lakes Can Increase Occurrence Frequency

MONIKA FELDMANN,[a,b,d] RICHARD ROTUNNO,[c] URS GERMANN,[b] AND ALEXIS BERNE[a]

[a] *Environmental Remote Sensing Laboratory, EPFL, Lausanne, Vaud, Switzerland*
[b] *Radar, Satellites and Nowcasting Division, MeteoSwiss, Locarno, Ticino, Switzerland*
[c] *Mesoscale and Microscale Meteorology Laboratory, NCAR, Boulder, Colorado*
[d] *Climate Impact Research—Oeschger Centre for Climate Change Research, University of Bern, Bern, Switzerland*

(Manuscript received 22 December 2022, in final form 18 October 2023, accepted 1 December 2023)

ABSTRACT: This study investigates the effects of lakes in mountainous terrain on the evolution of supercell thunderstorms. With a newly developed radar-based, mesocyclone-detection algorithm, a recent study has characterized the occurrence and evolution of supercell thunderstorms in the Swiss Alpine region. That study highlights the influence of orography on both storm intensity and occurrence frequency. To disentangle the different influential factors, an idealized modeling framework is established here using the mesoscale model CM1. The modeling scenarios are based on a high-CAPE environment with unidirectional shear, where a warm bubble serves to initiate the convection. Mimicking the environment of the southern Prealps in central Europe, scenarios with a high mountain ridge, valleys, and lakes are explored. The effect on the supercells of the slopes, high-altitude terrain, and moisture sources emphasizes the highly localized nature of terrain effects, leading to a heterogeneous intensity life cycle with transitory enhancement and weakening of the supercell. The dynamic and thermodynamic impact of mountain valleys with lakes increases the range of atmospheric conditions that supports supercellular development through horizontal vorticity production, increased storm relative helicity, and higher moisture content. This influence results in a systematic location dependence of the frequency, intensity, and lifetime of supercells, as also found in observations.

KEYWORDS: Convective storms; Convective-scale processes; Storm environments; Vorticity; Cloud resolving models; Idealized models

1. Introduction

The behavior of supercell thunderstorms in complex terrain is still poorly understood. Considering the high-impact nature of these storms (Hoeppe 2016; Ward et al. 2020) and the recent focus of field campaigns on areas of more complex topography (NSSL 2021; Nesbitt et al. 2021), we aim here to improve the understanding of how high-altitude terrain and topographic features such as lakes can affect a supercell's life cycle. Our focus lies on a localized supercell hotspot in the southern Prealps in central Europe (Feldmann et al. 2021, 2023). By reproducing key topographic features in a generalized manner in the idealized model CM1 (Bryan and Fritsch 2002), we aim to provide a conceptual model that details the general impacts of slopes and moisture sources.

The general processes behind supercell formation and the development of a mesocyclone are well known (Davies-Jones 2015; Markowski and Richardson 2010; Houze 2014). The tilting of horizontal vorticity in the atmospheric wind profile is one of the key contributors to the formation of a midlevel mesocyclone, in addition to a sufficient amount of convective available potential energy (CAPE), to generate a strong updraft.

Previous idealized studies focused on case studies (Homar et al. 2003), generalized idealized shapes (Markowski and Dotzek 2011; Ćurić et al. 2007) and the effects in climatological observations (Soderholm et al. 2014; Reeves and Lin 2007). More recent research has focused on the impact of terrain on convective environments (Katona et al. 2016; Lyza and Knupp 2018; Lyza et al. 2020; Katona and Markowski 2021). Even fewer studies target the influence of water bodies and moisture sources on convective storms. Wu and Lombardo (2021) investigated the impact of the marine boundary layer on quasi-linear convective systems in orographic coastal regions, but focus on the effects of the system encountering a stable boundary layer.

Most of these studies focus on severe storms in the United States, where supercells are most prevalent and tend to reach the highest intensities (Zipser et al. 2006). In contrast, Serafin et al. (2020) explored the effects of small-scale terrain features on a supercell in the Swiss and Austrian Alps with a case study, highlighting how small-scale terrain features play a key role in the maintenance of a favorable storm environment.

In this study we investigate the processes leading to supercell frequency clusters in the southern Prealps in a modeling framework. This area was also of key interest during the Mesoscale Alpine Programme (MAP) in 1999, where in the scope of an international field campaign, the importance of orographic precipitation enhancement in convection was

Denotes content that is immediately available upon publication as open access.

Feldmann's current affiliation: Institute of Geography, Oeschger Centre for Climate Change Research, University of Bern, Bern, Switzerland.

Corresponding author: Monika Feldmann, monika.feldmann@unibe.ch

DOI: 10.1175/MWR-D-22-0350.1

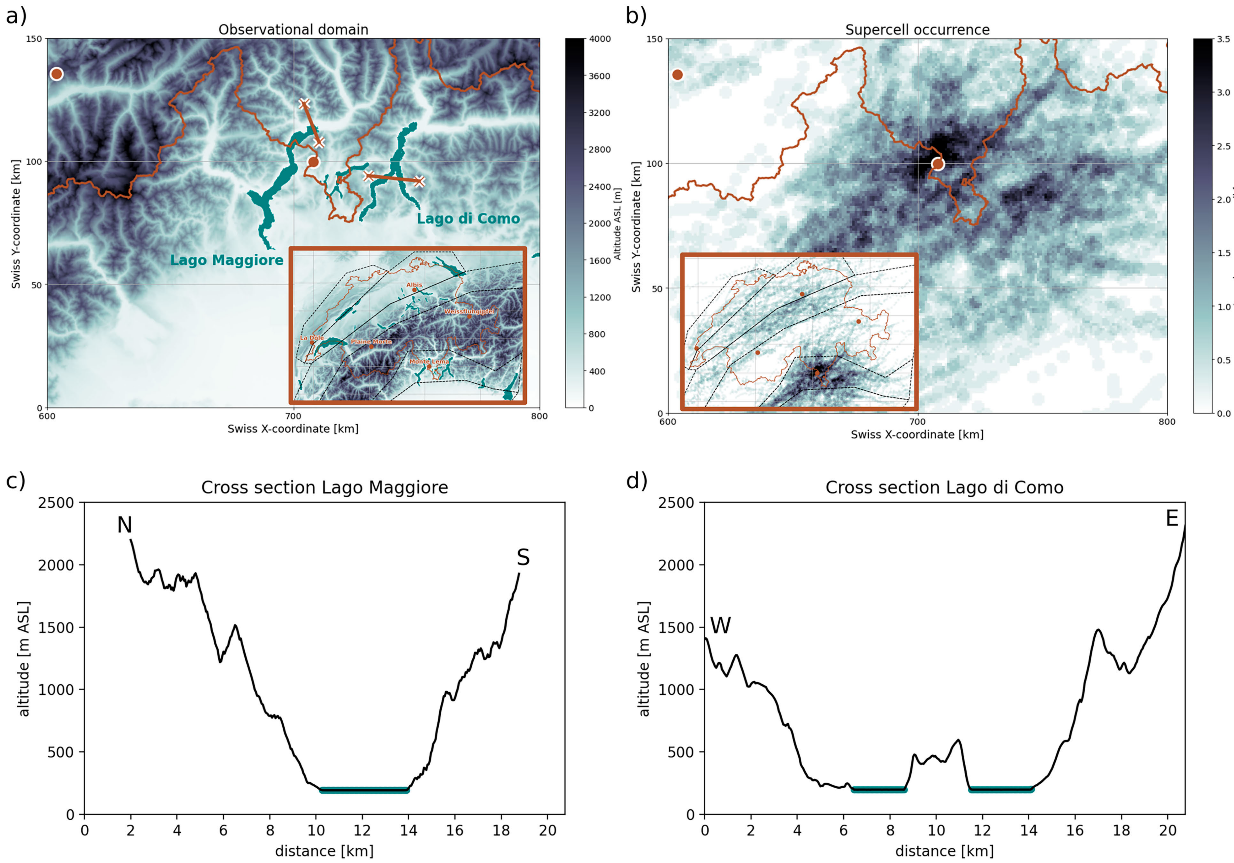

FIG. 1. (a) Topography of observational domain (swisstopo 2005; Jarvis et al. 2008), where radar locations are indicated with circles, and Swiss borders are marked with lines. (b) Supercell occurrence in (a). The small insets in (a) and (b) show the whole Swiss domain. (c),(d) Vertical cross sections, respectively, of Lago Maggiore and Lago di Como [indicated by the lines in (a)], with the lake marked in teal.

investigated (Rotunno and Ferretti 2003; Medina and Houze 2003; Rotunno and Houze 2007; Seity et al. 2003; Richard et al. 2003). Previous studies (Feldmann et al. 2021, 2023) have shown the occurrence of "hotspots" in valleys with large lakes. The southern prealpine lakes region is known for its severe thunderstorm prevalence (Manzato et al. 2022; Bagaglini et al. 2021) and the importance of the lakes often assumed (Ingemi 2023). The storm-intensity distribution in these areas is, however, lower than in the neighboring, flat, northwest Po valley, where fewer, but stronger supercells were observed (Feldmann et al. 2023). To investigate these findings, we derive modeling scenarios where the influential factors can be modified and allow the identification of causal relationships. We pursue an idealized approach, where we derive a simplified representation of the key conditions in the idealized mesoscale model CM1 (Bryan and Fritsch 2002). CM1 has been used for a number of supercell studies and is highly adaptable to the specific goals of a study. It has been used to study the effects of surface friction on tornadogenesis (Markowski 2016), high-resolution modeling of tornadoes (Orf et al. 2017), the effects of realistic terrain on supercell environments (Katona and Markowski 2021), the impact of idealized terrain features on supercell intensity (Markowski and Dotzek 2011), and, in combination with hail-trajectory models (Adams-Selin and Ziegler 2016; Kumjian and Lombardo 2020), the evolution of large and gargantuan hail in supercell life cycles (Kumjian et al. 2021) and environmental impact on storm severity (Lin and Kumjian 2022; Dennis and Kumjian 2017). Our setup differs from previous studies in the magnitude and arrangement of the terrain features and the inclusion of moisture sources. With a generalized setting the study is not limited to a single-case understanding. The present simplified approach also facilitates the identification of the underlying meteorological processes, allowing for the separation of lake-induced and topography-induced effects.

2. Model setup

In this section we present the observational data used to derive the idealized model setup, as well as the model setup itself.

a. Supercell observations in the Prealps

Previous studies in the Alpine region (Feldmann et al. 2020, 2021, 2023) have shown the occurrence of hotspots of supercells above the lakes of the southern Prealps, most notably in the northern portion of Lago Maggiore. Figure 1a

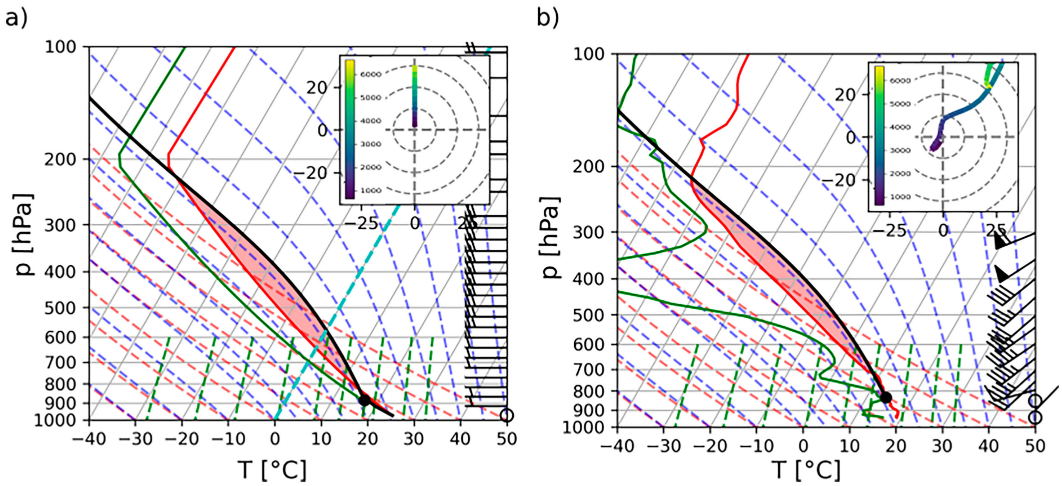

FIG. 2. (a) Initial sounding in the CM1 model; for illustrative purposes the model wind barbs are rotated 90°. (b) ERA5-based sounding from 0600 UTC 28 Jun 2022 in the vicinity of Lago Maggiore.

shows a topographical map of the southern Prealps and Fig. 1b the corresponding annual average supercell frequency, observed by the Swiss radar network. This convectively active area is also evident in Nisi et al. (2016), Punge et al. (2017), Nisi et al. (2018), Manzato et al. (2022). We aim here to identify the key environmental characteristics describing the region and then translate them into a generalized model setup.

The region considered here is a known hail hotspot (NCCS 2021), while tornadoes are uncommon (Sturmarchiv Schweiz 2021). The relevance of straight hodographs for hailstorms has been discussed in recent works (Kumjian and Lombardo 2020; Gutierrez and Kumjian 2021; Kumjian et al. 2021; Nixon and Allen 2022). Figure 2b shows an example of a simulated rawinsonde from ERA5 in the southern Prealps at 0600 UTC 28 June 2022. The hodograph indicates a southwesterly flow, increasing with altitude. There is barely any change in wind direction. The sounding reveals a CAPE of 2043 J kg^{-1} and a CIN of 1 J kg^{-1} and is associated with a severe hail-bearing supercell on the same day (Feldmann 2023).

b. Idealized numerical simulations

Based on the observations shown above, relevant scenarios are simulated using the idealized mesoscale model Cloud Model 1 (CM1) (Bryan and Fritsch 2002). The domain is $200 \times 300 \times 20$ km^3 (x, y, and z dimensions) with a horizontal grid spacing of 1×1 km^2 and 40 evenly spaced, terrain-following vertical levels. The lateral (east–west) boundaries are periodic, while an open-radiative condition is applied to the north–south boundaries to minimize wave reflection (Klemp and Wilhelmson 1978). The top of the domain has Rayleigh damping toward the base state, while the lower boundary is free slip. Although the grid spacing is coarse, the model is operated in large eddy simulation mode; subgrid-scale turbulence is modeled using the turbulent kinetic energy scheme (Deardorff 1980) and vertical turbulence tendencies are calculated implicitly via the Crank–Nicholson scheme. We use the Klemp–Wilhelmson compressible pressure solver (Klemp and Wilhelmson 1978) and the Morrison double-moment moisture scheme (Morrison et al. 2005). Since simulations are limited to a few hours and the domain is relatively small, we do not consider the Coriolis force. This setup follows previous terrain studies, such as Markowski and Dotzek (2011), Katona and Markowski (2021) and is focused on resolving storm-scale intensity behavior.

The observations shown in Fig. 2b and analyses of rawinsondes (Feldmann et al. 2023) and severe convective environments (Bagaglini et al. 2021) and case studies (Kopp et al. 2023; Avolio et al. 2020; Trefalt et al. 2018; Peyraud 2013) suggest we follow the steps of Markowski and Dotzek (2011) to set up a slightly drier Weisman–Klemp sounding (Weisman and Klemp 1982) by changing the exponent of the moisture function from 1.25 to 0.75. This results in a CAPE of 1974 J kg^{-1}, which represents the upper tail of the distribution of observed CAPE values in soundings associated with supercells in the region of interest, and a CIN of 25 J kg^{-1}. Considering the lack of directional shear, we transform the quarter-circle hodograph (Rotunno and Klemp 1982) by using the overall magnitude of wind speed in only the v direction. We hence maintain the magnitude of the vertical wind shear at 31 m s^{-1} over 0–6 km, but eliminate the directional component. The flow is aligned with the direction of the valleys, as the dominant flow direction during convective events in the target region is from the southwest (Feldmann et al. 2021) and aligned with the principal direction of the valley of Lago Maggiore and the western part of Lago di Como. The example shown in Fig. 2b demonstrates such a situation. Figure 2a depicts the analytical sounding used for model initiation. The thunderstorms in the simulation are initialized with a warm bubble (Markowski and Dotzek 2011).

c. Idealized topography

Cross sections of Lago Maggiore and Lago di Como in Figs. 1c and 1d highlight the steep topography immediately surrounding the lakes. The valleys in the southern Prealps are characterized by valley floors at a width of 10–20 km with the adjoining peaks rising 1500–2000 m above the valley floor. The key supercell hotspots also have lakes of considerable size. For example, Lago Maggiore is 65 km long and up to 10 km wide, Lago di Garda 50×17 km^2, Lago di Como 50×5 km^2 and Lago di Lugano 20×3 km^2.

To model this topography, we introduce a slope with a $\cos^2$ function up to 1500 and 2000 m, respectively, rising over a length of 50 km before plateauing in the center of the model domain given by (1). We perform experiments with both altitudes to see the influence of differing steepness and altitude. Following Lilly and Klemp (1979) the topography is brought back down to 0 m in the second half of the domain, to avoid producing a singularity in the wind field. In a second step, we introduce long, channel-shaped valleys into the slope. The valleys themselves also have slopes determined by a $\cos^2$ function and have a valley-floor width of 6.7 km and a peak-to-peak distance of 20 km. We opt to introduce a valley in both halves of the domain to compare the results with and without a lake in the same simulation. With the straight hodograph and no Coriolis force, the two split storms are mirrors of one another and can be directly compared. In the results this allows a separate discussion of effects caused by the orography and the lake.

The function of the slope is given by

$$h_{\mathrm{slope}}(y) = h_{\max}\cos^2\left[\pi\frac{(y - y_0)}{2y_1}\right], \tag{1}$$

where $h_{\max}$ is the peak altitude, y_0 is the offset of the peak, and y_1 is the length of the slope. Within the valleys, we superimpose a function sloping down from $h_{\mathrm{slope}}(y)$:

$$h_{\mathrm{valley}}(x, y) = h_{\mathrm{slope}}(y)\cos^2\left[\pi\frac{(x - x_0)}{2x_1}\right], \tag{2}$$

where x_0 is the edge of the slope before descending into the valley and x_1 is the width of the slope leading down to the valley floor.

Focusing on Lago Maggiore, we introduce a moisture ellipsoid the size of $60 \times 10 \times 1$ km^3. The height of the moisture perturbation (1000 m) is oriented relative to the height of the surrounding terrain, as indicated in Laiti et al. (2014). The magnitude of the moisture perturbation is also determined by the measurements taken in Laiti et al. (2014) over Lago di Garda. We reduce the undersaturation in the perturbed area by the same fraction as the measurements indicate (10%). Moreover, the moisture perturbation is maintained over the course of the simulation via a nudging term, representing the continuous evaporation over the lake.

The perimeter of the moisture perturbation is given by an ellipse:

$$\frac{x^2}{a^2} + \frac{y^2}{b^2} + \frac{z^2}{c^2} = 1. \tag{3}$$

For the inner core of the lake ($\mathrm{ell}_1 < 1$) a, b, and c are defined as follows: $a_1 = 3500$ m, $b_1 = 20\,000$ m, $c_1 = 500$ m. In a second, larger ellipse ($\mathrm{ell}_2 < 1$, $\mathrm{ell}_1 \geq 1$), the moisture perturbation decays linearly toward the background: $a_2 = 5000$ m, $b_2 = 30\,000$ m, and $c_2 = 1000$ m.

The perturbation in the initial conditions is confined to $\mathrm{ell}_2 < 1$:

$$Q_v(x, y, z) = Q_v(x, y, z) + \alpha(x, y, z)\Delta Q_v, \tag{4}$$

where $\mathrm{ell}_1 < 1$, $\alpha = 1$. However, in between the two ellipses, where $\mathrm{ell}_1 \geq 1$ and $\mathrm{ell}_2 < 1$, α is defined as the following:

$$\alpha(x, y, z) = 1 - \frac{\mathrm{ell}_2(x, y, z) - \mathrm{ell}_2(a_1, b_1, c_1)}{\mathrm{ell}_2(a_2, b_2, c_2) - \mathrm{ell}_2(a_1, b_1, c_1)}. \tag{5}$$

The nudging then maintains this perturbation where $\mathrm{ell}_2 < 1$:

$$\Delta Q_v(x, y, z, t) = Q_v(x, y, z, t = 0) - Q_v(x, y, z, t), \tag{6}$$

$$Q_v(x, y, z, t) = Q_v(x, y, z, t) + 0.8\Delta Q_v. \tag{7}$$

Figure 3 shows the final topographical setup in the full model domain including the slope up to 2000 m, the two valleys and the moisture source in the western valley. Comparing to Fig. 1, the dimensions of the topography in the model are also observed in the area. The results to follow are shown in the reduced area of the red box in Fig. 1a.

d. *Experimental summary*

In addition to the surface boundary conditions, the atmospheric initial conditions of the atmospheric profile are also varied. We reduce CAPE to approximately 1500 and 1000 J kg^{-1}, by reducing the temperature in the boundary layer by 1 K each and adjusting the moisture to maintain the relative humidity. Additionally, we reduce the 0–6-km shear to 25 and 20 m s^{-1}. An overview of all tested scenarios is given in Table 1. Simulation names are italicized throughout the results.

3. Analysis methods

To analyze the model output, we process the scenarios containing an initialized thunderstorm with the thunderstorm detection and tracking algorithm T-DaTing (Feldmann et al. 2021; PySteps developers 2021). By ingesting the composite reflectivity from the model output, the algorithm identifies reflectivity peaks above certain thresholds and identifies the contours at a lower reflectivity threshold using an inverse watershed algorithm (Beucher and Lantuejoul 1979; van der Walt et al. 2014). Utilizing optical flow (Lucas and Takeo 1981) computed over three previous time steps, the cell motion is estimated. Between time steps, detected cells are advected with their estimated motion and the overlap with cells detected in the next time step is computed to reidentify the same cells (Feldmann et al. 2021).

Since most thunderstorm-tracking algorithms struggle with cell splits [see also TRT (Hering et al. 2004), KONRAD3D (DWD 2022) or TITAN (NCAR 2022)], and we are working here with symmetrically splitting supercells, we simplify the tracking problem by splitting the domain in half and running T-DaTing independently in each half. This procedure yields reliable tracking results for all tested scenarios by using the default thunderstorm-tracking thresholds of this algorithm.

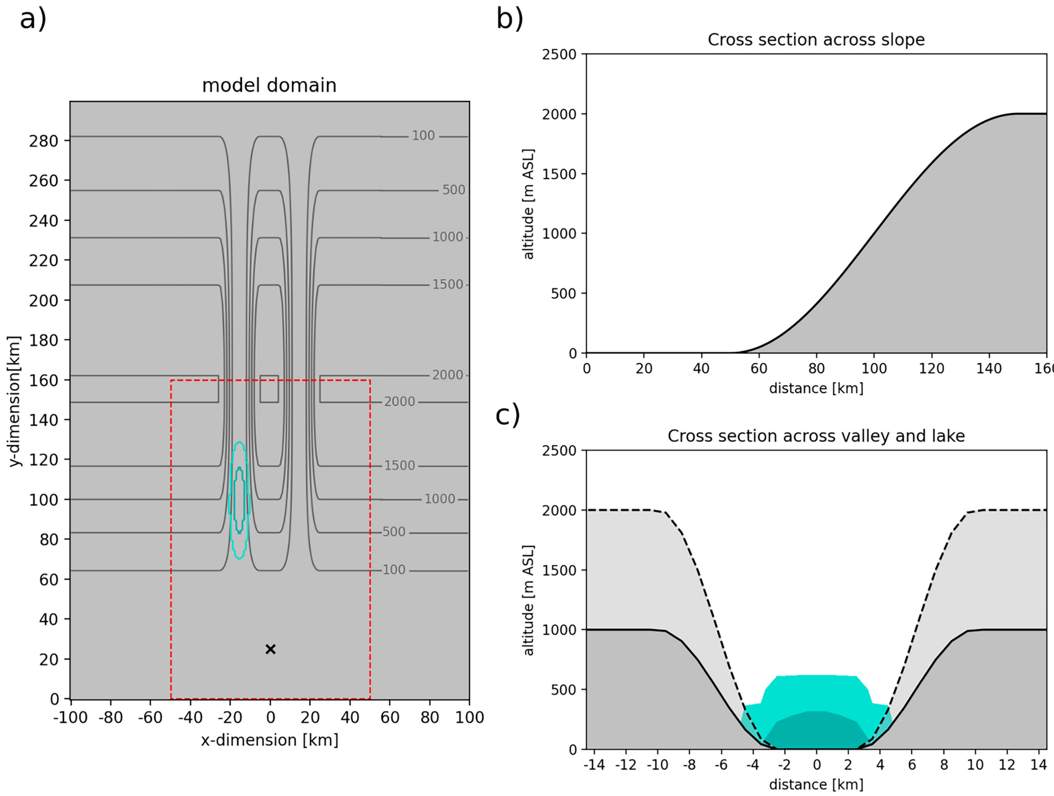

FIG. 3. Modeled topography for (a) full domain with key area for analyses shown in the red box, (b) cross section across the slope, and (c) cross section across the valley with the lake at y = 100 km (solid line and teal shading) and y = 150 km (dashed line), with the moisture perturbation shown in teal.

4. Results

a. Surface boundary conditions

In this first section we investigate the influence of terrain features on a supercell's life cycle, as shown in Figs. 4 and 5. Figure 4 shows the spatial evolution of successive 30-min time steps in the model for reflectivity, and vertical vorticity and updraft velocity at 4-km height, within the identified thunderstorm contours. Figure 5 shows the quantitative evaluation of the same variables every 5 min. The areas exceeding three separate thresholds are shown, where the bounds of the shaded area correspond to the outer thresholds and the solid

TABLE 1. Scenario descriptions; scenarios highlighted in results are noted with an asterisk and numbered in order.

	Scenario name	Topography	Lake	CAPE (J kg^{-1})	0–6-km shear (m s^{-1})	Various
	control* (1)	None	None	2000	31	
Surface boundary conditions	flat	None	None			
	slope* (2)	Slope to 2000 m	None			
	valley	2000-m valleys	None			
	lake_valley* (3)	2000-m valleys	Lake			
Atmospheric initial conditions	_med_cape			1500		
	_low_cape* (4)			1000		
	_med_shear				25	
	_low_shear* (5)				20	
Sensitivity tests	_1500	Max altitude 1500 m				
	_hr					Increased spatial resolution

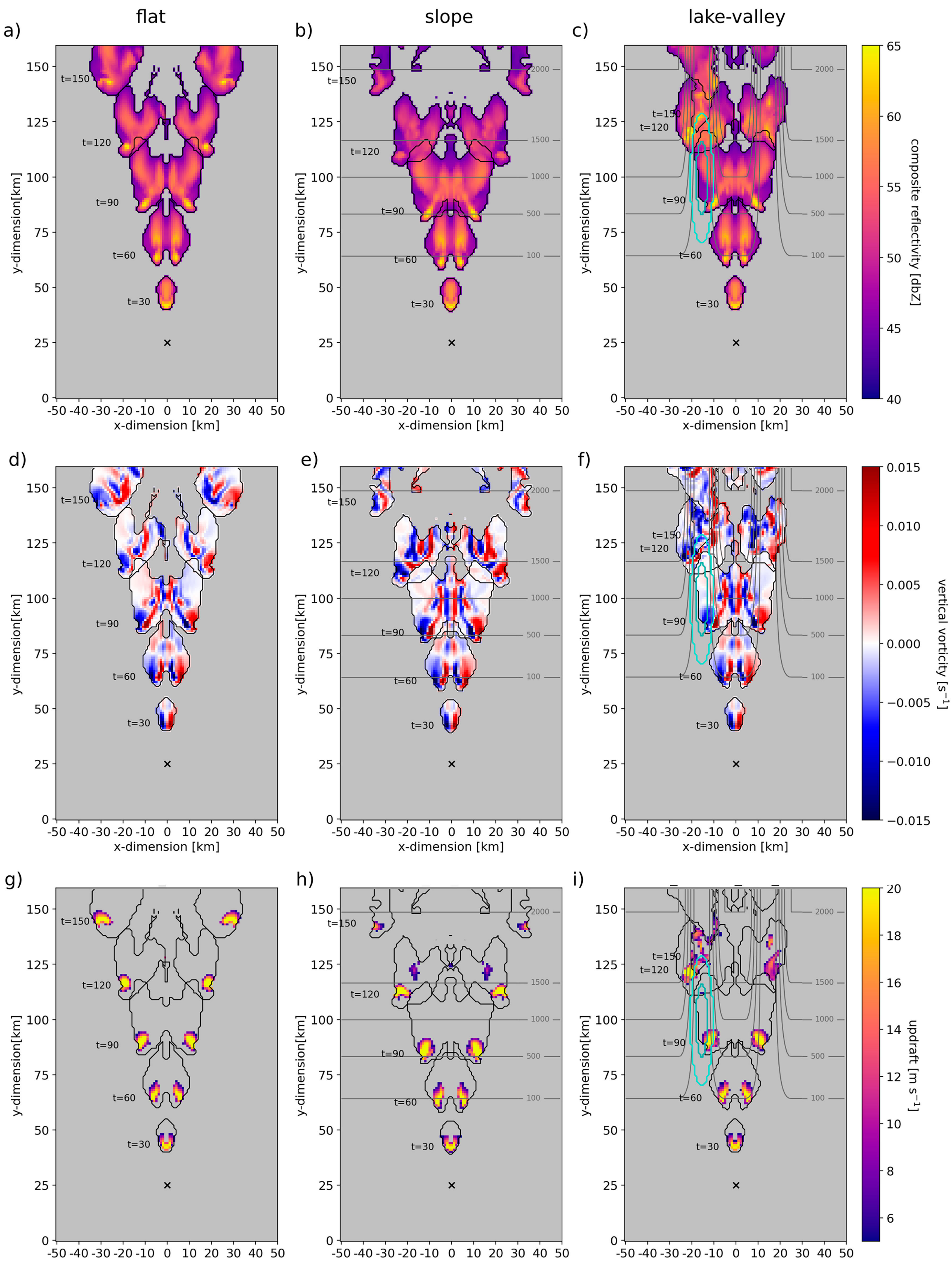

FIG. 4. Evolution of (a)–(c) reflectivity, (d)–(f) 4-km vertical vorticity, and (g)–(i) 4-km updraft > 5 m s^{-1} within thunderstorm contours every 30 min for the respective scenarios *control*, *slope*, and *valley_lake*. Isohypses are indicated in gray, the lake contour is indicated in teal, and the initiation location is indicated with a cross.

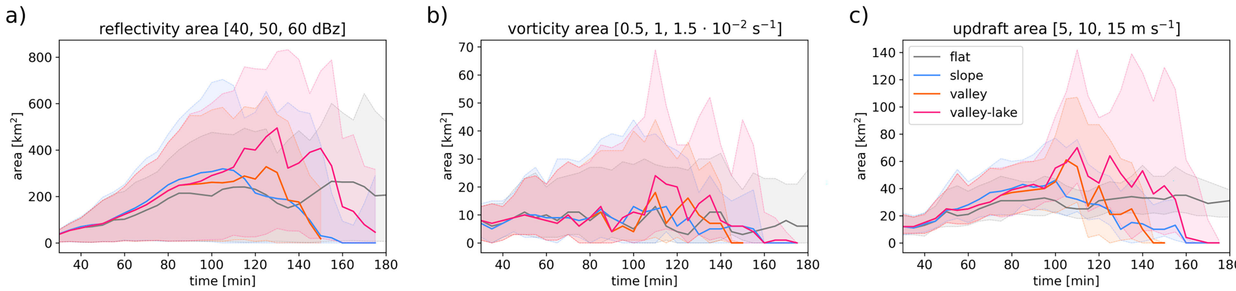

FIG. 5. Evolution of (a) reflectivity, (b) 4-km vertical vorticity within the updraft, and (c) 4-km updraft within thunderstorm contours for the respective scenarios *control*, *slope*, *valley*, and *valley_lake*. The bottom boundary of the shading refers to the highest threshold, the solid line refers to the medium threshold, and the top boundary refers to the lowest threshold.

line to the center threshold, allowing the evolution of each threshold to be inspected individually. The three separate thresholds generally show similar evolutions throughout the life cycles, but allow to investigate different intensity levels independently. Vertical vorticity is evaluated within the 5 m s^{-1} updraft area to focus on the mesocyclone strength. The control scenario using flat topography serves as a baseline. With unidirectional shear, and in the absence of the Coriolis force, the control run produces two mirror-symmetric, long-lived supercells—a left and a right mover (Figs. 4a,d,g). First looking at *slope* we can see that the symmetry is maintained, as expected (Figs. 4b,e,h); however, the supercells' life cycles are shortened (Fig. 5), as conditions at higher altitudes are unfavorable, with low CAPE and less moisture present. On the slope, near the 500-m contour at $t = 90$ min, there is an area where the supercells are locally enhanced. This difference is visible more clearly in the larger extent of high reflectivity, vorticity and updraft areas ranging over most of the storm life cycle, as shown in Fig. 5. The storm updraft is stronger over the slope (Figs. 4h and 5c). In this area, the background flow is already oriented upslope and the horizontal vorticity increases in magnitude, due to baroclinic vorticity production (see section 4b and Fig. 6). In addition, the most-unstable CAPE is based on parcels originating from slightly higher altitudes, so particularly the beginning of the slope has more favorable conditions and higher CAPE. This upslope enhancement in idealized simulations was also noted in Markowski and Dotzek (2011), although over much lower terrain with less pronounced slopes.

Moving toward the simulations including valleys, Figs. 4 and 5 show that in *valley* the supercells already exceed the intensity of *control* as long as they are within the valley. The eastern valley of the *valley_lake* scenario behaves very similarly to the scenario *valley*, we therefore only show the results of *valley_lake* in Figs. 4c, 4f, and 4i and discuss *valley* by focusing on the eastern valley without the lake. Upon encountering the lake ($t = 90$ min) and then the steep valley walls ($t = 120$ min), vorticity, updraft and precipitation rate are strongly enhanced. Once the storms fully reach the plateau, they rapidly decay in the less-favorable environment ($t \geq 120$ min), as also seen in the *slope* scenario. The increased storm intensity is confined to the valley and valley-entrance portion of the storm track.

b. Valley–lake enhancement of supercells

In this subsection we examine the influence of a valley and a valley with a lake on storm evolution as shown in Figs. 4c, 4f, and 4i. Figure 6a shows that the CAPE and moisture content are larger in the area of the lake. Figure 6b shows the effect of the topography on the ambient upstream flow; the horizontal wind vectors plotted on terrain-following coordinates indicate rising or sinking motion depending on whether the vectors point uphill or downhill, respectively. Away from the valley entrances there is rising motion on the plateau slope while there is slight sinking motion near the valley entrances. Comparing both valleys in Fig. 6b, we see that the lake causes no appreciable impact on the surface flow. The pattern of rising/sinking motion displaces isentropes vertically and produces the buoyancy pattern (at $z = 1250$ m) shown in Fig. 6c.

The horizontal vorticity associated with the ambient shear flow is a major factor in supercell dynamics (Davies-Jones 2015; Markowski and Richardson 2010; Houze 2014). In the present case the ambient flow $[0, V(z), 0]$ has the vorticity vector $(\xi, \eta, \zeta) = (-V_z, 0, 0)$, where the subscripts denote partial differentiation. Figure 6c shows the horizontal vorticity vector (ξ, η) at $z = 1250$ m; note that as the flow approaches the topography, ξ becomes more negative (greater vertical shear) and η develops such that horizontal vorticity vectors follow contours of constant buoyancy B. The relation between (ξ, η) and B can be explained by consideration of the vorticity equations given by

$$\frac{D\xi}{Dt} = \cdots + B_y, \tag{8}$$

$$\frac{D\eta}{Dt} = \cdots - B_x, \tag{9}$$

where D/Dt is the substantial derivative and the elided terms are small compared to the buoyancy gradient. It is clear from the foregoing equations that the decrease in ξ is a consequence of $B_y < 0$ in the topographically modified flow. The tendency of (ξ, η) to follow lines of constant B follows directly from the scalar product of (B_x, B_y) with the governing equations for (ξ, η), i.e., $B_x D\xi/Dt + B_y D\eta/Dt \approx 0$. A more general conclusion can be drawn from the conservation of potential

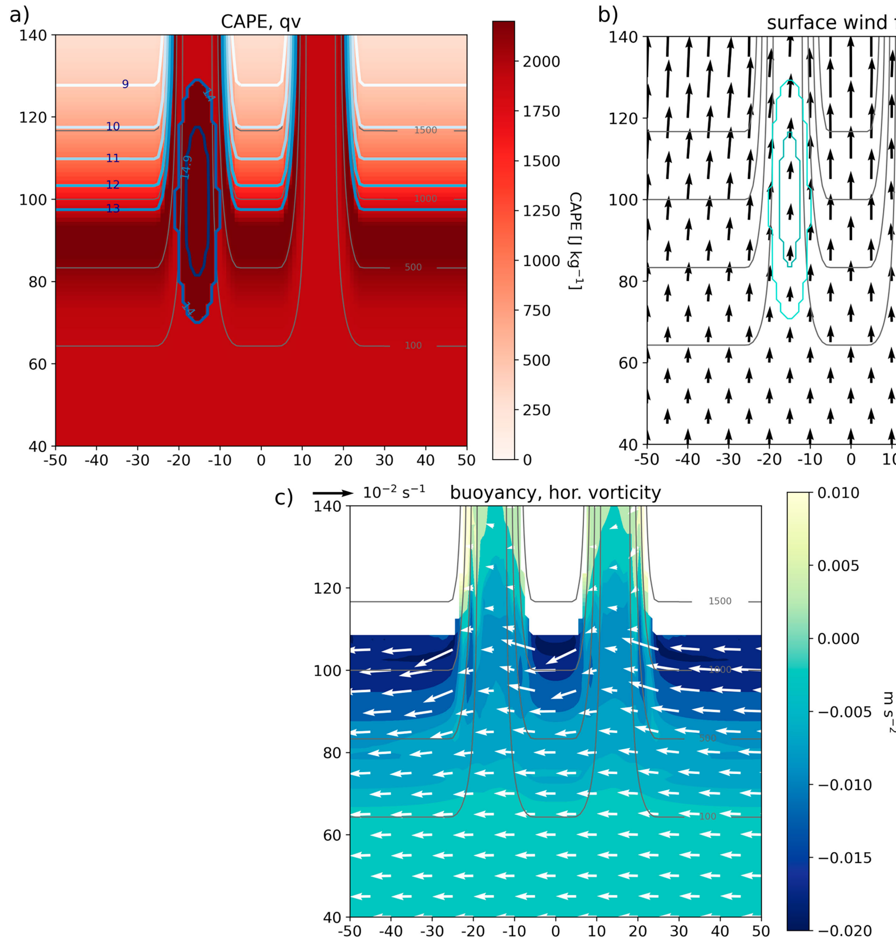

FIG. 6. Features of the *valley_lake* flow before convection initiation: (a) surface-based CAPE and water vapor mixing ratio in blue contours (g kg^{-1}), (b) horizontal flow at the surface, and (c) buoyancy at $z = 1250$ m with horizontal vorticity vectors superimposed.

vorticity ($\approx \xi B_x + \eta B_y + \zeta B_z = 0$; Ertel 1942) which, for $B_z > 0$, implies $\zeta > 0$ on the left and $\zeta < 0$ on the right side of the valley entrances. The ζ so produced was found to be small in comparison with the other factors in the supercell's vertical-vorticity generation.

To see how the terrain impacts supercell behavior, in Fig. 7 we compare flat-terrain supercells (left column) with those in the *valley_lake* case. Figure 7a shows the flat-terrain supercells which follow the standard development from a splitting initial cell in a straight-line hodograph (Rotunno and Klemp 1985). The storm structure exhibits the usual updraft–downdraft pairs moving across the ambient north-south shear with the downdraft divided into forward- and rear-flank parts. The flow field in the *valley_lake* case shown in Fig. 7b indicates the same features except for the forward-flank downdrafts which appear to be horizontally constrained by the valley walls. The horizontal constraint is due to the confinement of the cool air in the forward flank as indicated by comparing the buoyancy fields in Figs. 7c and 7d. As a result of this confinement the buoyancy gradient B_x is much stronger and, by virtue of (9), there is much stronger baroclinically produced vorticity. The higher horizontal vorticity and storm-relative flow, while being near alignment (Figs. 7e,f), produce much stronger storm-relative helicity in the *valley_lake* case and therefore stronger supercells compared to the flat-terrain case.

c. *Initial atmospheric conditions*

Following the topographical and lake experiments, we conduct a series of tests changing the initial atmospheric profile, as described in Table 1. First, we investigate how these changes affect the *control* scenario. We modify the initial sounding to lower the CAPE values to 1500 and 1000 J kg^{-1}, respectively. In *med_cape* (Figs. 8a,d,g and 9a–c) and *low_cape* (Figs. 9d–f) the storm intensity is reduced overall due to the reduced CAPE. The *low_cape* simulation shows a stronger decrease in intensity; however, the supercells still form as split storms and have significantly rotating updrafts, as shown in Figs. 9a–f. The deviation from the mean flow for the right and left mover is less pronounced than before, while the translational speed is not affected (Figs. 9g,h). The next series of tests utilizes the initial CAPE, but reduced deep shear to 25 and 20 m s^{-1}, respectively. In *med_shear* (Figs. 8b,e,h and 9a–c) and *low_shear* (Figs. 9d–f)

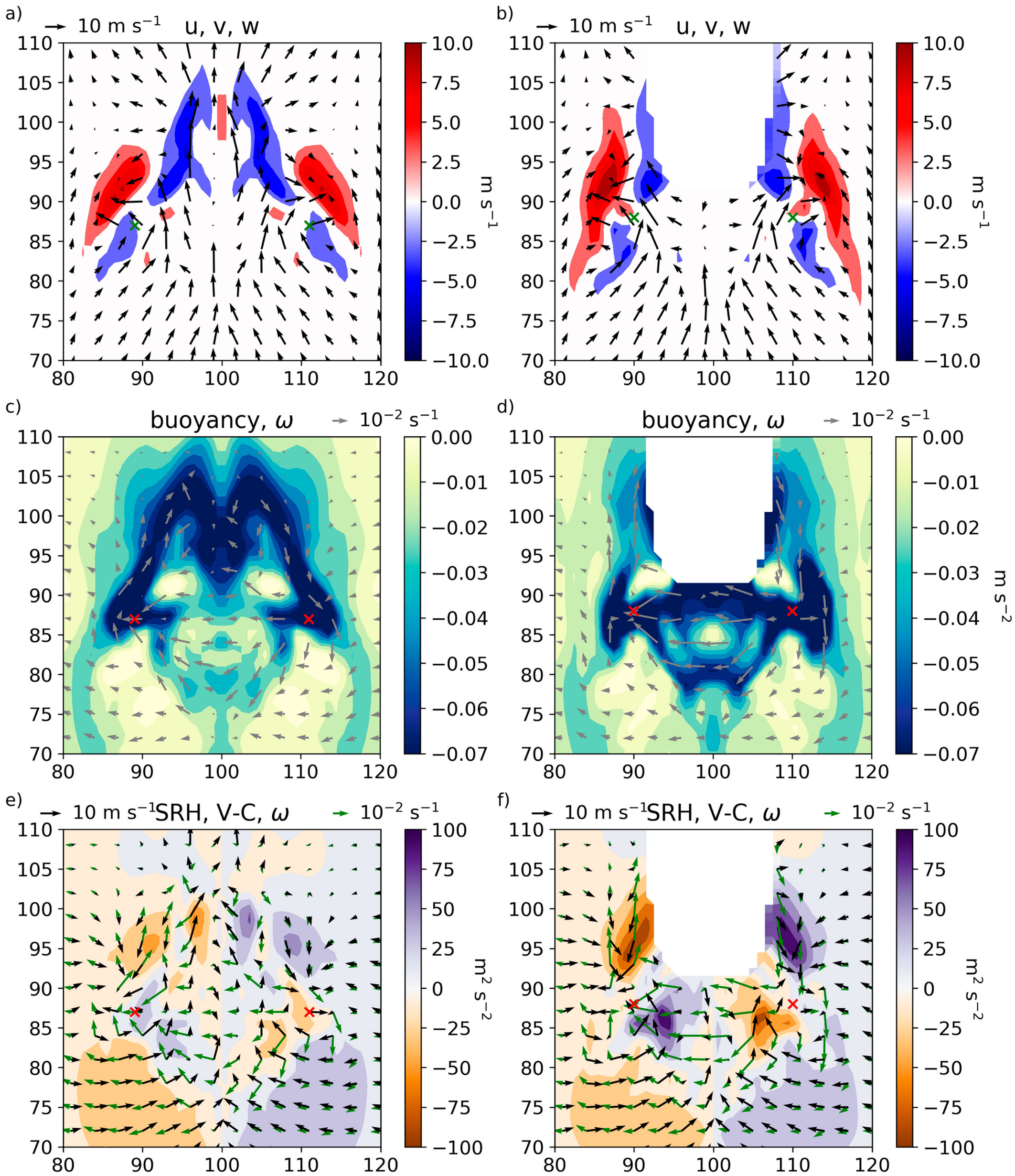

FIG. 7. Comparison of storm environment at $t = 90$ min, $z = 1250$ m with (left) flat terrain and (right) lake and valley. (a),(b) Horizontal flow in black vectors and vertical velocity in contours; (c),(d) buoyancy at 1250 m and horizontal vorticity in gray vectors; (e),(f) storm relative helicity (SRH) over 500 m in contours, storm-relative flow in black vectors, and horizontal vorticity in green vectors. The storm centroids are indicated with crosses, the area is windowed in to the area of the storm.

we see the effects of lower vertical shear on the evolution of the *control* scenario. With the midlevel flow being weaker, the overall translational speed is reduced (Fig. 9g). Moreover the lower shear results in a less-pronounced deviation of storm motion from the mean flow (Davies-Jones 2015; Bunkers et al. 2000) (Fig. 9h). With decreasing shear, the overall storm intensity also decreases and the lifetime shortens. Particularly the *low_shear* scenario shows a much shorter lifetime, together with a strongly reduced storm area and overall reduced intensity. Overall, the supercells react more sensitively to the applied changes in deep shear than to the change in CAPE described above. Figures 8c, 8f, and 8i show the combination of both effects, with moderately reduced CAPE and shear (1500 J kg^{-1} and 25 m s^{-1}, *med_cape_shear*). In this case the cells form, split and are persistent. Figure 9g shows that the translational speed is slower than in the *control* case, but not as slow as in the *low_shear* case. The deviation from the mean flow is also less pronounced than in the *control* scenario (Fig. 9h).

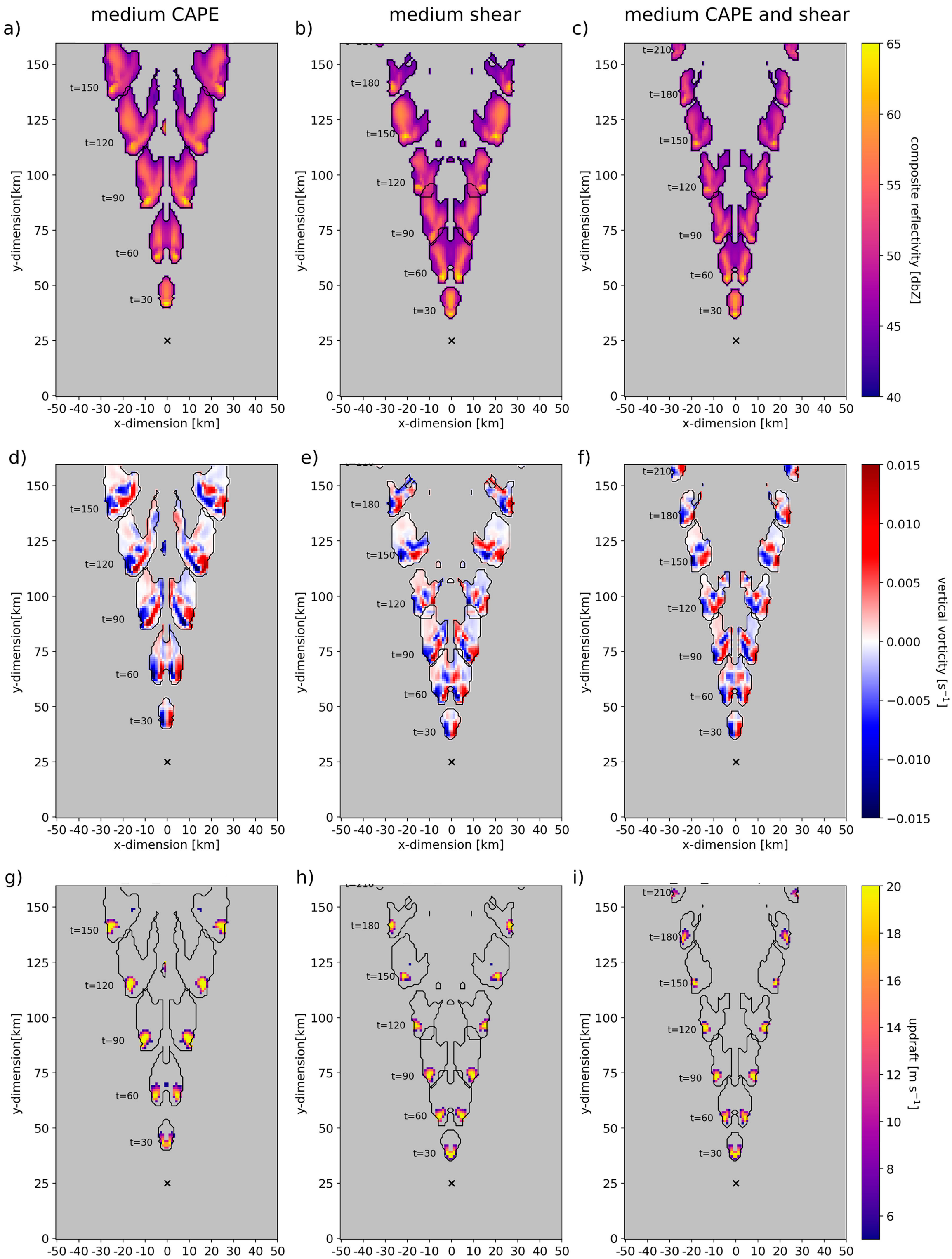

FIG. 8. Evolution of (a)–(c) reflectivity, (d)–(f) 4-km vertical vorticity, and (g)–(i) 4-km updraft > 5 m s^{-1} within thunderstorm contours every 30 min for the respective scenarios *med_cape*, *med_shear*, and *med_cape_shear*. Isohypses are indicated in gray, the lake contour is indicated in teal, and the initiation location is indicated with a cross.

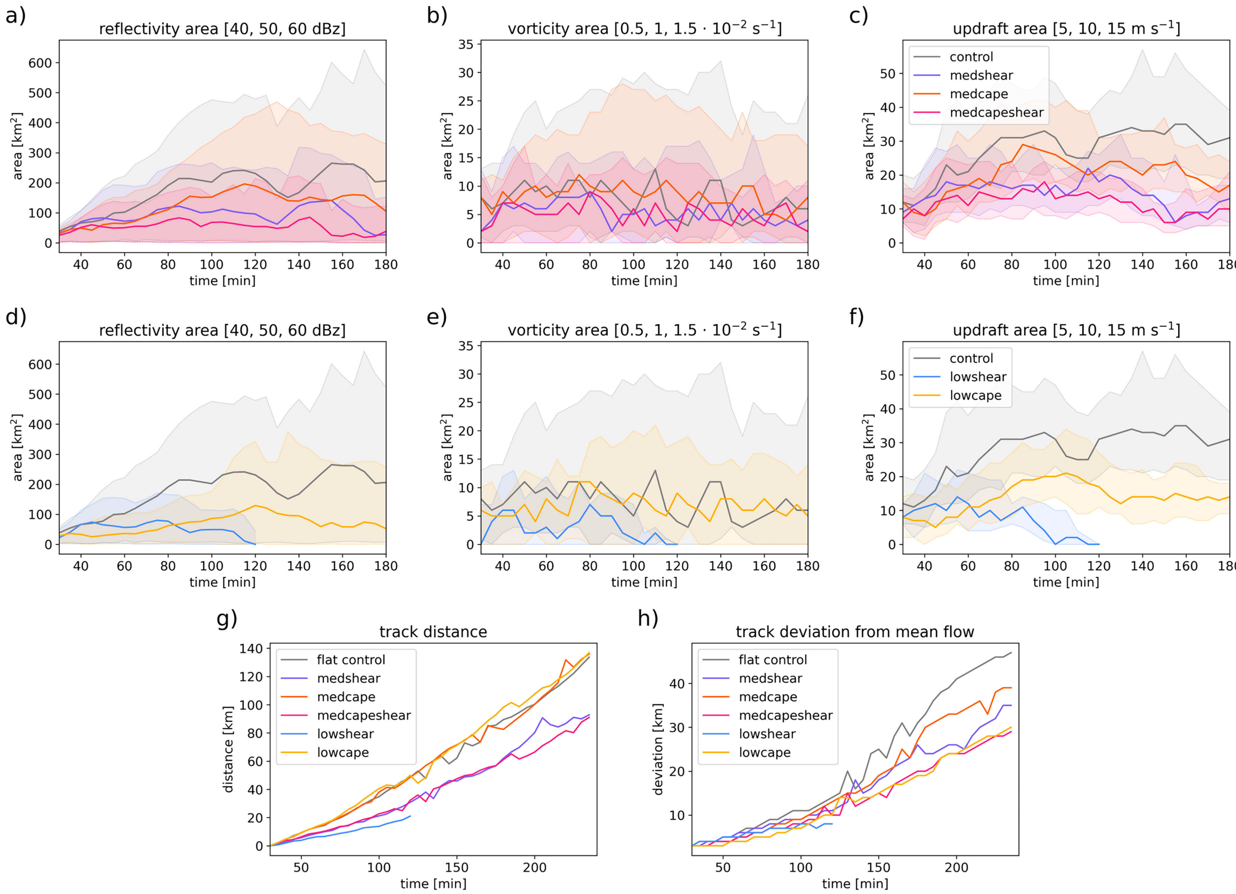

FIG. 9. Evolution of (a),(d) reflectivity; (b),(e) 4-km vertical vorticity within the updraft; (c),(f) 4-km updraft; (g) cumulative distance of track; and (h) cumulative track deviation within thunderstorm contours for the respective scenarios *med_cape*, *med_shear*, *med_cape_shear*, *low_cape*, and *low_shear*. The bottom boundary of the shading refers to the highest threshold, the solid line refers to the medium threshold, and the top boundary refers to the lowest threshold.

The overall intensity of the storms is still strongly reduced, with peak updraft and updraft area smaller than in the *control* case (Figs. 9a–f). When strongly reducing both CAPE and deep shear (1000 J kg^{-1} and 20 m s^{-1}, *low_cape_shear*), the cells no longer fully form and the environment no longer supports deep convection (tracking no longer activates).

We now investigate the same modifications for the *valley_lake* scenario. When adding topography and a lake, *valley_med_cape* (Figs. 10a,d,g and 11a–c) and *valley_low_cape* (Figs. 11d–f) also show consistent intensity reductions. In these cases, the supercells form and split into symmetrical pairs (aside from the influence of the lake). Since the reduced-CAPE scenarios have a weaker updraft (Figs. 11c,e), the resulting track deviation (Fig. 11h) is also less pronounced. The presence of the lake does enhance the magnitude and area of the updraft subsequently, but does not compensate for the overall reduction in CAPE.

The reduced-shear scenarios *valley_med_shear* (Figs. 10b,e,h and 11a–c) and *valley_low_shear* (Figs. 11d–f) are also able to produce deep convection with significant rotation. The evolution of both reduced-shear scenarios is notably stronger than in the *control* scenarios with reduced shear, longer lifetime, higher reflectivity values, a larger spatial extent of the storm and higher vorticity values. This applies both to the valley with and without a lake. Considering Figs. 6 and 7, the topography of the valleys is key for the generation of additional SRH.

When combining both modifications here into the *valley_med_cape_shear* scenario, we see the importance of both the thermodynamic and dynamic modifications of lake and valley (Figs. 10c,f,i). The case *valley_med_cape_shear* shows distinctly stronger cells both with the lake and without it, but the eastern cell no longer reaches the plateau due to the narrower track. It hence does not fully encounter the valley sidewall. The western cell intensifies after crossing the lake, producing a stronger updraft and higher precipitation rates. It still reaches the plateau and later decays. The combination of both increased vorticity and CAPE in the western valley leads to a storm that locally intensifies to vorticity, updraft and precipitation values similar to the *valley_lake* scenario. The case *valley_low_cape_shear* also does not support a full storm evolution, but the weak convection forming is longer-lasting than in the *low_cape_shear* case (not shown here).

Overall, the reductions in CAPE and shear lead to a reduced storm intensity, but to a lesser extent than in the flat case. The

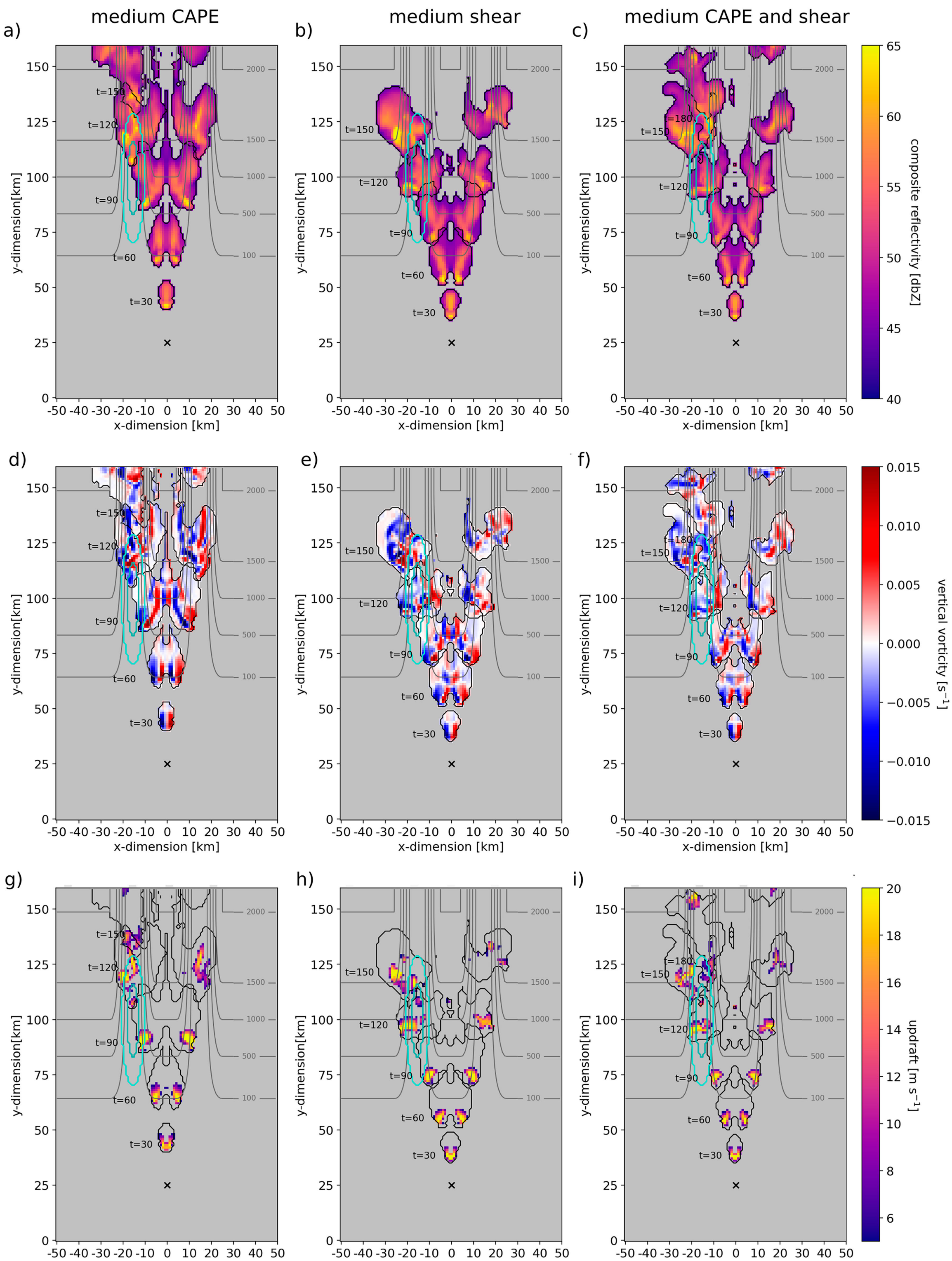

FIG. 10. Evolution of (a)–(c) reflectivity, (d)–(f) 0–5-km vertical vorticity, and (g)–(i) 0–5-km updraft > 5 m s^{-1} within thunderstorm contours every 30 min for the respective scenarios *valley_med_cape*, *valley_med_shear*, and *valley_med_cape_shear*. Isohypses are indicated in gray, the lake contour is indicated in teal, and the initiation location is indicated with a cross.

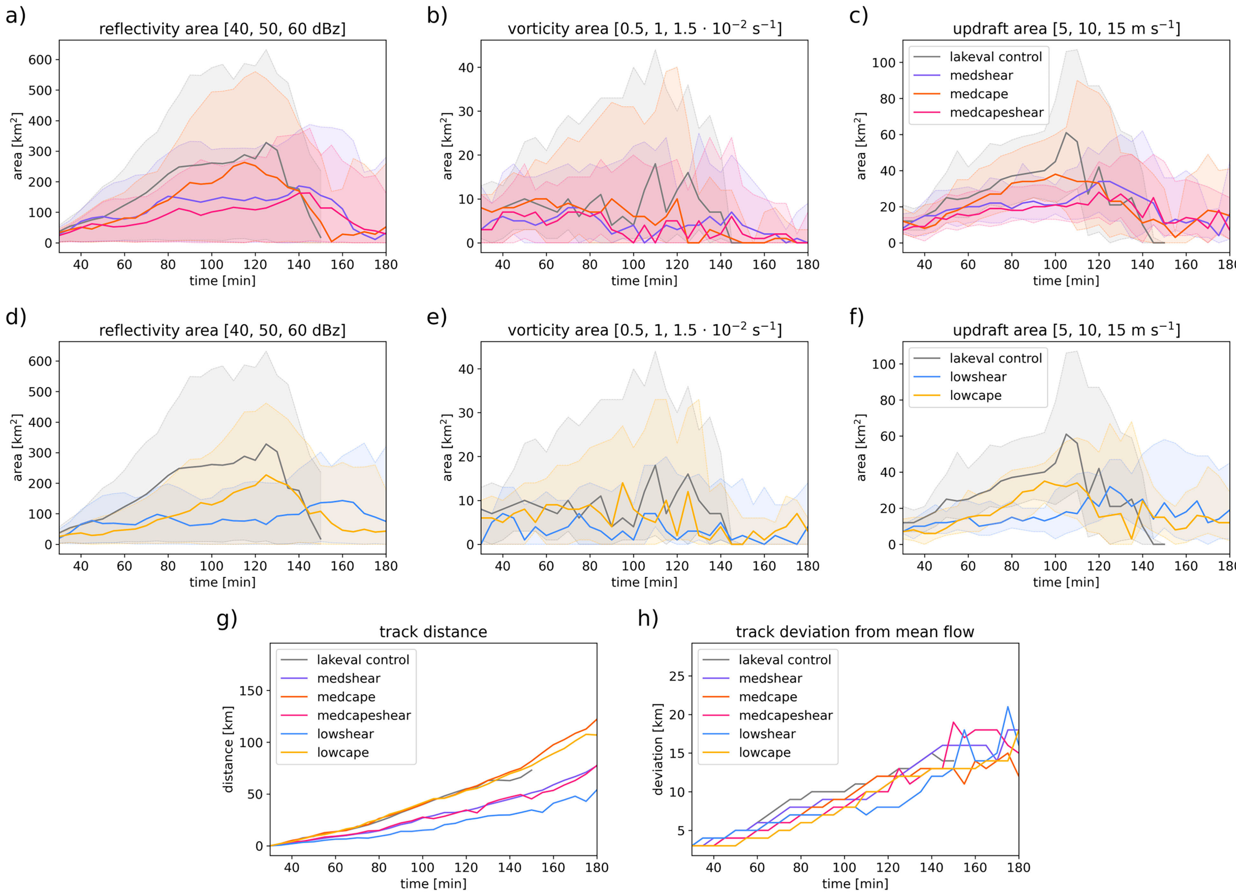

FIG. 11. Evolution of (a),(d) reflectivity; (b),(e) 4-km vertical vorticity within the updraft; (c),(f) 4-km updraft; (g) cumulative distance of track; and (h) cumulative track deviation within thunderstorm contours for the *valley_lake* scenarios *med_cape*, *med_shear*, *med_cape_shear*, *low_cape*, and *low_shear*. The bottom boundary of the shading refers to the highest threshold, the solid line refers to the medium threshold, and the top boundary refers to the lowest threshold.

comparison of Figs. 9 and 11 shows that the supercells in lake valleys react less sensitively to the initial conditions of the simulation.

d. Sensitivity tests

A number of sensitivity tests were performed on the valley shape, the width/steepness of the slopes and the size and magnitude of the lake as a moisture source. The tests with different terrain setups revealed that supercell evolution is sensitive to the steepness of a slope, but as long as it is not excessively steep, the slope-influenced vertical motion, increase in horizontal vorticity and locally enhanced CAPE will locally support the storm's intensification.

The life cycle evolutions for the scenarios *slope*, *valley*, and *lake_valley* are compared to *slope_1500*, *valley_1500*, and *lake_valley_1500* in Fig. 12. The lower terrain leads to a less pronounced intensification and a smaller weakening of the updraft on the plateau. However, the changes are small in nature and the differences between the principal scenarios *slope*, *valley*, and *lake_valley* exceed the effect of changing terrain altitude.

Valleys narrowing toward the end have a more pronounced confluence effect and a stronger effect on the vertical velocity at their end. When varying the terrain altitude, strong responses were seen in the updraft velocity and precipitation accumulation starting from ridge heights around 2500 m, likely originating from the orographic effects of the increasingly steep valley walls. These altitude differences no longer correspond to the region of interest and hence were not explored further.

While the size of the lake and strength of its moisture perturbation are taken from observations, we also experimented with larger sizes and modified perturbations. Increasing or decreasing the initial perturbation leads to a proportional response in precipitation rate. However, changing the size of the lake or the nature of the maintained nudging has a stronger effect on the outcome. Increasing the size increases the overall amount of moisture that is additionally available which results in a larger volume that is nudged and further increases the available moisture. The nudging is the most sensitive part of the setup since it affects every computational time step and changes accumulate throughout the simulation. When reducing the nudging to the lowest model layer, the outcome is very similar.

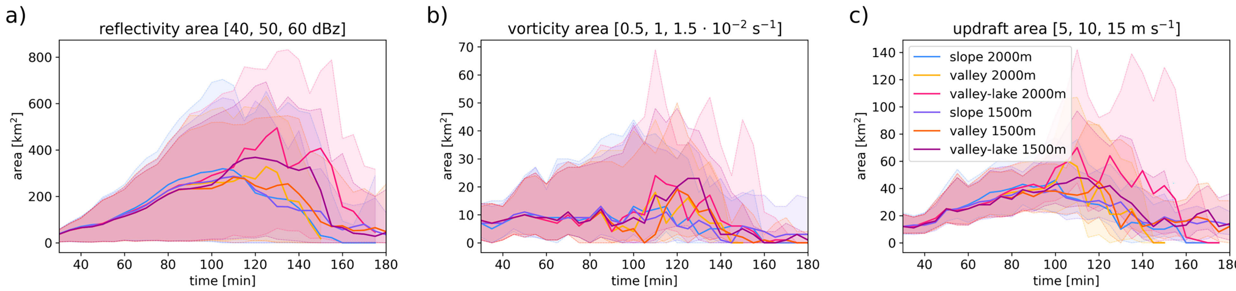

FIG. 12. Evolution of (a) reflectivity, (b) 4-km vertical vorticity within the updraft, and (c) 4-km updraft within thunderstorm contours for the respective scenarios *slope_1500*, *valley_1500*, and *valley_lake_1500* in comparison to their 2000-m counterparts. The bottom boundary of the shading refers to the highest threshold, the solid line refers to the medium threshold, and the top boundary refers to the lowest threshold.

However, when turning off the nudging entirely, the initial perturbation is moved with the flow, gets absorbed into an overpassing storm and hence dissipates. The storm will still experience strengthening, but to a much lesser degree, as the additional moisture is much lower. A moisture perturbation that is too strong will produce a circulation that in itself disturbs the organization of deep convection. In this case, where the perturbation produces no perceptible circulation (see Fig. 6b), the results we believe are realistic.

To assess the robustness of the results with respect to model resolution, a selection of scenarios was repeated with an increased horizontal grid spacing of 200 m × 200 m, stretching in the outer domain to 500 m × 500 m, and terrain-following vertical levels with a low-level grid spacing of 100 m, stretching to 500 m at higher altitudes. The higher resolution allows for more pronounced extremes at smaller scales, leading to some quantitative differences. However, the qualitative differences between the scenarios remain the same, with slopes locally enhancing updraft and storm strength, high altitude being detrimental, the lake increasing updraft area and precipitation rate and the slope and valleys promoting an increased horizontal vorticity leading to greater SRH. The life cycle evolution for the scenarios *flat_hr*, *slope_hr*, *valley_hr*, and *lake_valley_hr* are shown in Fig. 13. The main mechanisms discussed before remain the same.

5. Discussion

The comparison of supercells evolving in flat terrain, up a slope and through valleys with a lake has revealed localized intensification and weakening caused by the terrain. In the *slope* scenario, there is a localized intensification midslope, where CAPE is higher; CAPE decreases with further increases in altitude to the top of the plateau and consequently storms decay. This locally higher CAPE was found over the (much lower) mountains studied in Katona and Markowski (2021). Likewise, Markowski and Dotzek (2011) identifies upslope enhancement through reduction of CIN and moisture accumulation. Both the present study and Markowski and Dotzek (2011), Katona and Markowski (2021) support the concept of the very localized nature of terrain impacting storm intensity.

The comparison of weaker convective environments with and without terrain has shown that supercell thunderstorms are able to persist in less conducive environments in topography, even if their intensity is not as high as in the *control* case. Particularly the lower-shear environments are of interest here. In the simulations without initiated storms, we can identify areas of increased horizontal vorticity along the valley sides. These stem from perturbed isotherms that induce baroclinic vorticity generation. The channeling into the valley also leads to an increased horizontal wind speed further up the valley. The perturbed flow occurs with additional vertical shear on the principal slope that is not present in the *control* simulation. Once the supercell encounters the valley entrance, the terrain constrains the forward-flank downdraft to a smaller area, creating greater buoyancy gradients and further increasing the baroclinically generated vorticity (Rotunno and Klemp 1985).

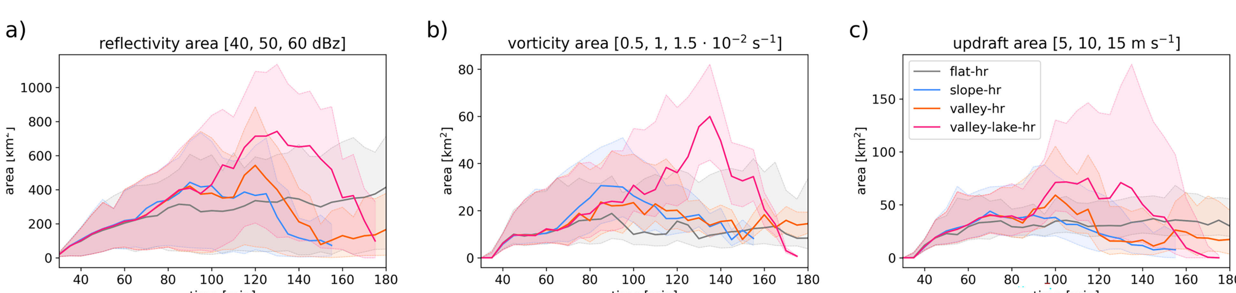

FIG. 13. Evolution of (a) reflectivity, (b) 4-km vertical vorticity within the updraft, and (c) 4-km updraft within thunderstorm contours for the respective scenarios *control-hr*, *slope-hr*, *valley-hr*, and *valley_lake-hr*. The bottom boundary of the shading refers to the highest threshold, the solid line refers to the medium threshold, and the top boundary refers to the lowest threshold.

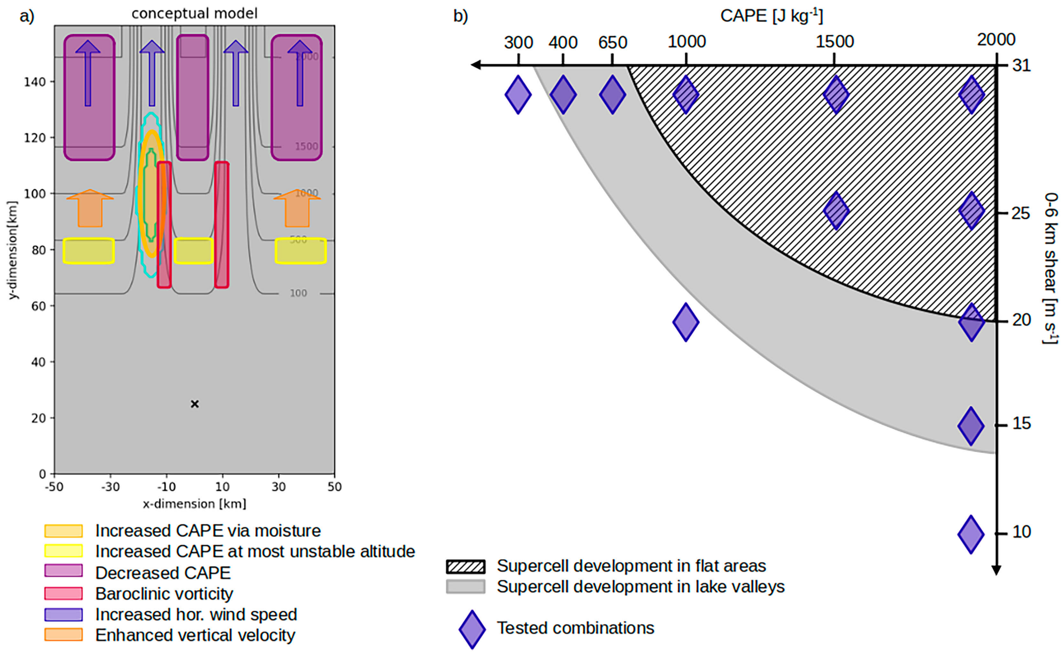

FIG. 14. (a) Conceptual model of the dynamic and thermodynamic effects affecting supercell evolution in valleys with lakes. (b) CAPE and shear environments leading to supercell development in differing topography.

The aligned inflow and vorticity yield large values of SRH, that positively impact the overall intensity (Davies-Jones 1984; Dahl 2017; Coffer et al. 2023). Subsequently the storms encountering the valley have larger updrafts and mesocyclones. This additional baroclinic vorticity compensates the lack of vorticity in a low-shear environment without topography. The presence of the lake in these simulations impacts the thermodynamic lower boundary conditions, CAPE is greater through the higher moisture content. So air stemming from the lake entering the storm has a greater potential to rise, increasing the strength and size of the updraft, thus enabling the tilt of a greater portion of the horizontal vorticity (Markowski and Dotzek 2011; Weisman and Klemp 1982). This indicates that especially valleys with lakes are able to sustain supercell thunderstorms in conditions that no longer support their full development without topography, which is in agreement with the findings of Feldmann et al. (2021, 2023).

To explore the limits of supercell occurrence in the modeled scenarios, we further reduce CAPE down to 300 J kg^{-1} and 0–6-km shear to 10 m s^{-1}. In flat terrain at 31 m s^{-1} deep shear, supercells stop occurring at CAPE levels below 800 J kg^{-1}. In valleys with lakes, supercells only stop occurring at CAPE values below 400 J kg^{-1}. As shown in Fig. 8, in flat terrain at 2000 J kg^{-1} CAPE, supercells stop forming below 20 m s^{-1} deep shear. Supercells in valleys with lake persist well in environments with deep shear as low as 15 m s^{-1}, which is below the generally mentioned deep-shear requirement of 20 m s^{-1} for supercell evolution (Markowski and Richardson 2010). They finally no longer form at 10 m s^{-1} deep shear. In all of these scenarios the valley without lake also shows supercellular development, where the valley with lake does, but with a weaker intensity. Overall, both the flat and valley configuration are more sensitive to changes in deep shear than in CAPE. This concurs with studies on high-shear, low-CAPE supercell evolution (e.g., Wade and Parker 2021).

Figure 14a gives an overview of the identified processes. Figure 14b additionally gives an overview of the results, which conditions support supercellular development in flat terrain in contrast to valleys with lakes. We see here the wider range of initial conditions leading to supercell evolution in valleys with lakes, in comparison to flat terrain.

The importance of topography for vorticity generation was also found in Markowski and Dotzek (2011), Ćurić et al. (2007), Homar et al. (2003). Especially small-scale features have an important role in maintaining a favorable environment, as supported by case studies (Scheffknecht et al. 2017; Homar et al. 2003; LeBel et al. 2021). Increased low-level vorticity through orographic channeling of flow that leads to mesocyclone intensification was also found in case studies in California, New York, and Massachusetts, albeit in wider valleys with less steep surrounding terrain (Braun and Monteverdi 1991; LaPenta et al. 2005; Bosart et al. 2006). Studies investigating preferential tornado formation near terrain features (Lyza and Knupp 2018; Lyza et al. 2020) point out the importance of low-level SRH amplification in certain flow situations. The SRH amplification is due to low-level flow enhancement, while in the *valley* scenario we see a combination of inflow enhancement and baroclinic vorticity production. Markowski and Dotzek (2011) highlights the upslope enhancement of convection and how topography induces heterogeneity in the atmospheric environment. Moreover, the topographic generation of vorticity anomalies in valley-flow situations is shown. Rotunno and Klemp (1985) discusses the importance of baroclinic vorticity in the inflow area for low-level rotation in supercells, which we see enhanced in the *valley* scenario.

The effect of the lake is mainly represented by increased CAPE and equivalent potential temperature (θ_e) in the environment. The impact of CAPE on the storm intensity and updraft is also discussed in Lin and Kumjian (2022), Peters et al. (2020), Markowski and Dotzek (2011), Weisman and Klemp (1982). The role of topography in maintaining higher θ_e environments is also examined in Scheffknecht et al. (2017), LeBel et al. (2021), Mulholland et al. (2019). The key combination here is the higher θ_e environment from the lake inside the topographic setting with the valley. The valley walls channel the flow, reducing the source of inflow air to the valley, where the lake is located. The subsequent higher moisture content in the storm increases the precipitation rate, which is further enhanced orographically when encountering the slope (Houze 2012).

Overall, here we combine several aspects of topographic influence, where both dynamic and thermodynamic perturbations play a role. The findings agree with previous studies that also reflect on these aspects and support the supercell frequency distribution found in observations in the area.

6. Conclusions

In this work we analyze the evolution of idealized supercell simulations in different topographic and environmental settings. We aim to explore the meteorological processes leading to observed high frequencies of supercell occurrence in Prealpine valleys with lakes on the southern side of the Swiss Alps. With the scenarios explored here we can isolate the effects stemming from topography from those of the lakes. The topographic experiments show a localized enhancement of the updraft, when the supercell is moving upslope. In addition, the vertical vorticity signature is more pronounced in these areas. At lower altitudes of the slopes, the environment is very favorable with even higher CAPE values than in the absence of topography, supporting the localized enhancement. At higher altitudes, the environment becomes increasingly unfavorable, with decreasing CAPE and decreasing moisture content. In all scenarios the supercells decay once they reach the high altitude plateau of 1500–2000 m.

The presence of valleys leads to a modification of the horizontal flow. On the slopes next to the valleys, the flow converges into the valley with an initial downslope motion. This introduces heterogeneity in the u and v field, that leads to additional horizontal vorticity. Inside the valley, the channeled flow has a higher velocity. The perturbed flow over the topography perturbs the isopycnes and leads to baroclinic production of horizontal vorticity on the principal slope and at the valley walls. Furthermore, the valley walls constrain the forward flank downdraft, which leads to higher baroclinicity and vorticity. The channeling effect of the valley increases the inflow speed and producing high SRH. Large SRH is a known factor to positively impact storm-scale intensity (Davies-Jones 1984; Dahl 2017; Coffer et al. 2023), as seen in the larger areas of updraft, vorticity and reflectivity. Once the storm moves over the steep valley sides, its updraft is further enhanced until it reaches the plateau and subsequently decays.

The presence of a lake provides the supercells with additional moisture and energy. While not perturbing the initial flow, it induces an area of elevated CAPE, leading to a larger and stronger updraft. The storm also has a larger area of elevated vorticity, indicating a stronger mesocyclone. The additional moisture increases the precipitation rate. These effects of the lake compound with the effects of topography.

Experiments with modifications of the initial environmental conditions show that overall the supercells react more strongly to modifications of the vertical shear profile, than a reduction in CAPE. The scenarios including topography are less sensitive to a reduction in vertical shear, as the orographic-flow-induced baroclinicity provides additional horizontal vorticity to compensate for the lack of shear. While not quite reaching the same peak intensity, supercells are able to form and subsist in conditions, where they no longer persist in the experiments without topography. The addition of a lake with the resulting larger updraft further bolsters this robustness.

Overall the longest supercell life cycle with high constant intensity is found in the control simulation without topography and high CAPE and shear values. However, the scenarios with topography and lake show localized pronounced intensification of the storms during their passage through the valleys and over upslope portions of the terrain. The life cycles are shortened by the decay on the high-altitude plateau. The influence of terrain and lakes on supercell results in a systematic location dependence of the frequency, intensity and lifetime of supercells. In addition, these scenarios are less sensitive to reductions in vertical shear, indicating that supercells can persist in a wider range of environmental conditions.

Considering the observational background, that supercells in the southern Prealps are more frequent than those in the flat northwest Po Valley, the investigated scenarios support this observation. The Po Valley is very wide and flat, leading to no topographic effects impacting the supercells occurring within it. They hence have longer life cycles at a high and more constant intensity. The narrower valleys of Lago Maggiore and Lago di Como are similar to the topographic scenarios tested here and support supercell occurrence in a wider range of initial conditions. Life cycles are usually shorter and have a more heterogeneous intensity evolution than in the Po Valley. We conclude that the additional vorticity induced by orographic flow locally provides favorable conditions for supercell persistence, while moisture sources and upslope portions can locally intensify a storm considerably.

By identifying new thresholds for larger-scale environmental shear for foothill regions of mountains, climatological studies may utilize reanalysis data to derive the frequency of severe convective environments. Specifically for the southern Prealps, such an analysis may yield a longer record of supercell occurrence than the current, radar-based dataset (Feldmann et al. 2021, 2023).

Acknowledgments. We thank Dr. George Bryan for his assistance and advice in setting up and handling CM1 simulations.

The collaboration of M. Feldmann and R. Rotunno is supported by the EDCE Mobility grant of EPFL and the Graduate Visitor Program of the National Center for Atmospheric Research. The contribution of R. Rotunno to this work is supported by the National Center for Atmospheric Research, which is a major facility sponsored by the National Science Foundation under Cooperative Agreement 1852977.

Data availability statement. The simulations were conducted with the open-source model Cloud Model 1 (CM1) (Bryan and Fritsch 2002) and can be obtained through https://www2.mmm.ucar.edu/people/bryan/cm1/.

REFERENCES

Adams-Selin, R. D., and C. L. Ziegler, 2016: Forecasting hail using a one-dimensional hail growth model within WRF. *Mon. Wea. Rev.*, **144**, 4919–4939, https://doi.org/10.1175/MWR-D-16-0027.1.

Avolio, E., L. Nisi, L. Panziera, L. Peyraud, and M. M. Miglietta, 2020: A multi-sensor and modeling analysis of a severe convective storm in Lake Maggiore area (northwestern Italy). *Atmos. Res.*, **242**, 105008, https://doi.org/10.1016/j.atmosres.2020.105008.

Bagaglini, L., R. Ingrosso, and M. M. Miglietta, 2021: Synoptic patterns and mesoscale precursors of Italian tornadoes. *Atmos. Res.*, **253**, 105503, https://doi.org/10.1016/j.atmosres.2021.105503.

Beucher, S., and C. Lantuejoul, 1979: Use of watersheds in contour detection. *Int. Workshop on Image Processing: Real-time Edge and Motion Detection/Estimation*, Rennes, France, 17–21, https://people.cmm.minesparis.psl.eu/users/beucher/publi/watershed.pdf.

Bosart, L. F., A. Seimon, K. D. LaPenta, and M. J. Dickinson, 2006: Supercell tornadogenesis over complex terrain: The Great Barrington, Massachusetts, tornado on 29 May 1995. *Wea. Forecasting*, **21**, 897–922, https://doi.org/10.1175/WAF957.1.

Braun, S. A., and J. P. Monteverdi, 1991: An analysis of a mesocyclone-induced tornado occurrence in northern California. *Wea. Forecasting*, **6**, 13–31, https://doi.org/10.1175/1520-0434(1991)006<0013:AAOAMT>2.0.CO;2.

Bryan, G. H., and J. M. Fritsch, 2002: A benchmark simulation for moist nonhydrostatic numerical models. *Mon. Wea. Rev.*, **130**, 2917–2928, https://doi.org/10.1175/1520-0493(2002)130<2917:ABSFMN>2.0.CO;2.

Bunkers, M. J., B. A. Klimowski, J. W. Zeitler, R. L. Thompson, and M. L. Weisman, 2000: Predicting supercell motion using a new hodograph technique. *Wea. Forecasting*, **15**, 61–79, https://doi.org/10.1175/1520-0434(2000)015<0061:PSMUAN>2.0.CO;2.

Coffer, B. E., M. D. Parker, J. M. Peters, and A. R. Wade, 2023: Supercell low-level mesocyclones: Origins of inflow and vorticity. *Mon. Wea. Rev.*, **151**, 2205–2232, https://doi.org/10.1175/MWR-D-22-0269.1.

Ćurić, M., D. Janc, and V. Vučković, 2007: Numerical simulation of Cb cloud vorticity. *Atmos. Res.*, **83**, 427–434, https://doi.org/10.1016/j.atmosres.2005.10.024.

Dahl, J. M. L., 2017: Tilting of horizontal shear vorticity and the development of updraft rotation in supercell thunderstorms. *J. Atmos. Sci.*, **74**, 2997–3020, https://doi.org/10.1175/JAS-D-17-0091.1.

Davies-Jones, R., 1984: Streamwise vorticity: The origin of updraft rotation in supercell storms. *J. Atmos. Sci.*, **41**, 2991–3006, https://doi.org/10.1175/1520-0469(1984)041<2991:SVTOOU>2.0.CO;2.

——, 2015: A review of supercell and tornado dynamics. *Atmos. Res.*, **158–159**, 274–291, https://doi.org/10.1016/j.atmosres.2014.04.007.

Deardorff, J. W., 1980: Stratocumulus-capped mixed layers derived from a three-dimensional model. *Bound.-Layer Meteor.*, **18**, 495–527, https://doi.org/10.1007/BF00119502.

Dennis, E. J., and M. R. Kumjian, 2017: The impact of vertical wind shear on hail growth in simulated supercells. *J. Atmos. Sci.*, **74**, 641–663, https://doi.org/10.1175/JAS-D-16-0066.1.

DWD, 2022: Thunderstorm detection and tracking with KONRAD. Deutscher Wetterdienst, accessed 24 October 2022, https://www.dwd.de/EN/research/weatherforecasting/met_applications/nowcasting/konrad_en_node.html.

Ertel, H., 1942: Über das verhältnis des neuen hydrodynamischen wirbelsatzes zum zirkulationssatz von v. bjerknes (in German). *Meteor. Z.*, **59**, 385–387.

Feldmann, M., 2023: Supercell thunderstorms in the Alpine region—From weather radar observations to idealized modeling. M.S. thesis, Lausanne, EPFL, 178 pp., https://doi.org/10.5075/epfl-thesis-10232.

——, C. N. James, M. Boscacci, D. Leuenberger, M. Gabella, U. Germann, D. Wolfensberger, and A. Berne, 2020: R2D2: A region-based recursive Doppler dealiasing algorithm for operational weather radar. *J. Atmos. Oceanic Technol.*, **37**, 2341–2356, https://doi.org/10.1175/JTECH-D-20-0054.1.

——, U. Germann, M. Gabella, and A. Berne, 2021: A characterisation of Alpine mesocyclone occurrence. *Wea. Climate Dyn.*, **2**, 1225–1244, https://doi.org/10.5194/wcd-2-1225-2021.

——, A. Hering, M. Gabella, and A. Berne, 2023: Hailstorms and rainstorms versus supercells—A regional analysis of convective storm types in the Alpine region. *npj Climate Atmos. Sci.*, **6**, 19, https://doi.org/10.1038/s41612-023-00352-z.

Gutierrez, R. E., and M. R. Kumjian, 2021: Environmental and radar characteristics of gargantuan hail–producing storms. *Mon. Wea. Rev.*, **149**, 2523–2538, https://doi.org/10.1175/MWR-D-20-0298.1.

Hering, A. M., C. Morel, G. Galli, S. Sénési, P. Ambrosetti, and M. Boscacci, 2004: Nowcasting thunderstorms in the Alpine region using a radar based adaptive thresholding scheme. *Proc. ERAD Conf. 2004*, Visby, Sweden, Copernicus, 206–211, https://www.copernicus.org/erad/2004/online/ERAD04_P_206.pdf.

Hoeppe, P., 2016: Trends in weather related disasters—Consequences for insurers and society. *Wea. Climate Extremes*, **11**, 70–79, https://doi.org/10.1016/j.wace.2015.10.002.

Homar, V., M. Gayà, R. Romero, C. Ramis, and S. Alonso, 2003: Tornadoes over complex terrain: An analysis of the 28th August 1999 tornadic event in eastern Spain. *Atmos. Res.*, **67–68**, 301–317, https://doi.org/10.1016/S0169-8095(03)00064-4.

Houze, R. A., Jr., 2012: Orographic effects on precipitating clouds. *Rev. Geophys.*, **50**, RG1001, https://doi.org/10.1029/2011RG000365.

——, 2014: Clouds and precipitation associated with hills and mountains. *Cloud Dynamics*, R. A. Houze, Ed., International Geophysics Series, Vol. 104, Academic Press, 369–402, https://doi.org/10.1016/B978-0-12-374266-7.00012-3.

Ingemi, D., 2023: La caratteristica dei forti temporali che si originano con una certa frequenza sopra il lago di Garda. MeteoWeb, accessed 25 May 2023, https://www.meteoweb.eu/2012/

06/la-caratteristica-dei-forti-temporali-che-si-originano-con-una-certa-frequenza-sopra-il-lago-di-garda/139421/.

Jarvis, A., E. Guevara, H. I. Reuter, and A. D. Nelson, 2008: Hole-filled SRTM for the globe: Version 4: Data grid. CGIAR Consortium for Spatial Information, accessed 3 May 2021, http://srtm.csi.cgiar.org.

Katona, B., and P. Markowski, 2021: Assessing the influence of complex terrain on severe convective environments in northeastern Alabama. *Wea. Forecasting*, **36**, 1003–1029, https://doi.org/10.1175/WAF-D-20-0136.1.

——, ——, C. Alexander, and S. Benjamin, 2016: The influence of topography on convective storm environments in the eastern United States as deduced from the HRRR. *Wea. Forecasting*, **31**, 1481–1490, https://doi.org/10.1175/WAF-D-16-0038.1.

Klemp, J. B., and R. B. Wilhelmson, 1978: The simulation of three-dimensional convective storm dynamics. *J. Atmos. Sci.*, **35**, 1070–1096, https://doi.org/10.1175/1520-0469(1978)035<1070:TSOTDC>2.0.CO;2.

Kopp, J., K. Schröer, C. Schwierz, A. Hering, U. Germann, and O. Martius, 2023: The summer 2021 Switzerland hailstorms: Weather situation, major impacts and unique observational data. *Weather*, **78**, 184–191, https://doi.org/10.1002/wea.4306.

Kumjian, M. R., and K. Lombardo, 2020: A hail growth trajectory model for exploring the environmental controls on hail size: Model physics and idealized tests. *J. Atmos. Sci.*, **77**, 2765–2791, https://doi.org/10.1175/JAS-D-20-0016.1.

——, ——, and S. Loeffler, 2021: The evolution of hail production in simulated supercell storms. *J. Atmos. Sci.*, **78**, 3417–3440, https://doi.org/10.1175/JAS-D-21-0034.1.

Laiti, L., D. Zardi, M. de Franceschi, G. Rampanelli, and L. Giovannini, 2014: Analysis of the diurnal development of a lake-valley circulation in the Alps based on airborne and surface measurements. *Atmos. Chem. Phys.*, **14**, 9771–9786, https://doi.org/10.5194/acp-14-9771-2014.

LaPenta, K. D., L. F. Bosart, T. J. Galarneau Jr., and M. J. Dickinson, 2005: A multiscale examination of the 31 May 1998 Mechanicville, New York, tornado. *Wea. Forecasting*, **20**, 494–516, https://doi.org/10.1175/WAF875.1.

LeBel, L. J., B. H. Tang, and R. A. Lazear, 2021: Examining terrain effects on an upstate New York tornado event utilizing a high-resolution model simulation. *Wea. Forecasting*, **36**, 2001–2020, https://doi.org/10.1175/WAF-D-21-0018.1.

Lilly, D. K., and J. B. Klemp, 1979: The effects of terrain shape on nonlinear hydrostatic mountain waves. *J. Fluid Mech.*, **95**, 241–261, https://doi.org/10.1017/S0022112079001452.

Lin, Y., and M. R. Kumjian, 2022: Influences of CAPE on hail production in simulated supercell storms. *J. Atmos. Sci.*, **79**, 179–204, https://doi.org/10.1175/JAS-D-21-0054.1.

Lucas, B. D., and T. Kanade, 1981: An iterative image registration technique with an application to stereo vision. *Proc. Seventh Int. Joint Conf. on Artificial Intelligence (IJCAI '81)*, Vancouver, BC, Canada, Morgan Kaufmann Publishers Inc., 674–679, https://www.ri.cmu.edu/pub_files/pub3/lucas_bruce_d_1981_1/lucas_bruce_d_1981_1.pdf.

Lyza, A. W., and K. R. Knupp, 2018: A background investigation of tornado activity across the southern Cumberland Plateau terrain system of northeastern Alabama. *Mon. Wea. Rev.*, **146**, 4261–4278, https://doi.org/10.1175/MWR-D-18-0300.1.

——, T. A. Murphy, B. T. Goudeau, P. T. Pangle, K. R. Knupp, and R. A. Wade, 2020: Observed near-storm environment variations across the southern Cumberland Plateau system in northeastern Alabama. *Mon. Wea. Rev.*, **148**, 1465–1482, https://doi.org/10.1175/MWR-D-19-0190.1.

Manzato, A., S. Serafin, M. M. Miglietta, D. Kirshbaum, and W. Schulz, 2022: A pan-Alpine climatology of lightning and convective initiation. *Mon. Wea. Rev.*, **150**, 2213–2230, https://doi.org/10.1175/MWR-D-21-0149.1.

Markowski, P. M., 2016: An idealized numerical simulation investigation of the effects of surface drag on the development of near-surface vertical vorticity in supercell thunderstorms. *J. Atmos. Sci.*, **73**, 4349–4385, https://doi.org/10.1175/JAS-D-16-0150.1.

——, and Y. Richardson, 2010: *Mesoscale Meteorology in Midlatitudes*. John Wiley and Sons, Ltd, 430 pp., https://doi.org/10.1002/9780470682104.

——, and N. Dotzek, 2011: A numerical study of the effects of orography on supercells. *Atmos. Res.*, **100**, 457–478, https://doi.org/10.1016/j.atmosres.2010.12.027.

Medina, S., and R. A. Houze Jr., 2003: Air motions and precipitation growth in Alpine storms. *Quart. J. Roy. Meteor. Soc.*, **129**, 345–371, https://doi.org/10.1256/qj.02.13.

Morrison, H., J. A. Curry, and V. I. Khvorostyanov, 2005: A new double-moment microphysics parameterization for application in cloud and climate models. Part I: Description. *J. Atmos. Sci.*, **62**, 1665–1677, https://doi.org/10.1175/JAS3446.1.

Mulholland, J. P., S. W. Nesbitt, and R. J. Trapp, 2019: A case study of terrain influences on upscale convective growth of a supercell. *Mon. Wea. Rev.*, **147**, 4305–4324, https://doi.org/10.1175/MWR-D-19-0099.1.

NCAR, 2022: Thunderstorm Identification, Tracking, Analysis, and Nowcasting (TITAN). NCAR, accessed 24 October 2022, https://ral.ucar.edu/solutions/products/thunderstorm-identification-tracking-analysis-and-nowcasting-titan.

NCCS, 2021: Hail Climate Switzerland—National hail hazard maps. National Centre for Climate Services brochure Tech. Rep., 8 pp., https://www.meteosuisse.admin.ch/dam/jcr:3275b0ba-d179-4076-ad0f-d909e7ea4bc2/NCCS_Brochure_Hail_Climate_Switzerland_EN.pdf.

Nesbitt, S. W., and Coauthors, 2021: A storm safari in subtropical South America: Proyecto RELAMPAGO. *Bull. Amer. Meteor. Soc.*, **102**, E1621–E1644, https://doi.org/10.1175/BAMS-D-20-0029.1.

Nisi, L., O. Martius, A. Hering, M. Kunz, and U. Germann, 2016: Spatial and temporal distribution of hailstorms in the Alpine region: A long-term, high resolution, radar-based analysis. *Quart. J. Roy. Meteor. Soc.*, **142**, 1590–1604, https://doi.org/10.1002/qj.2771.

——, A. Hering, U. Germann, and O. Martius, 2018: A 15-year hail streak climatology for the Alpine region. *Quart. J. Roy. Meteor. Soc.*, **144**, 1429–1449, https://doi.org/10.1002/qj.203286.

Nixon, C. J., and J. T. Allen, 2022: Distinguishing between hodographs of severe hail and tornadoes. *Wea. Forecasting*, **37**, 1761–1782, https://doi.org/10.1175/WAF-D-21-0136.1.

NSSL, 2021: VORTEX southeast. NOAA/NSSL, accessed 23 September 2021, https://www.nssl.noaa.gov/projects/vortexse/.

Orf, L., R. Wilhelmson, B. Lee, C. Finley, and A. Houston, 2017: Evolution of a long-track violent tornado within a simulated supercell. *Bull. Amer. Meteor. Soc.*, **98**, 45–68, https://doi.org/10.1175/BAMS-D-15-00073.1.

Peters, J. M., H. Morrison, C. J. Nowotarski, J. P. Mulholland, and R. L. Thompson, 2020: A formula for the maximum vertical velocity in supercell updrafts. *J. Atmos. Sci.*, **77**, 3747–3757, https://doi.org/10.1175/JAS-D-20-0103.1.

Peyraud, L., 2013: Analysis of the 18 July 2005 tornadic supercell over the Lake Geneva region. *Wea. Forecasting*, **28**, 1524–1551, https://doi.org/10.1175/WAF-D-13-00022.1.

Punge, H. J., K. M. Bedka, M. Kunz, and A. Reinbold, 2017: Hail frequency estimation across Europe based on a combination of overshooting top detections and the ERA-INTERIM reanalysis. *Atmos. Res.*, **198**, 34–43, https://doi.org/10.1016/j.atmosres.2017.07.025.

pySTEPS Developers, 2021: pySTEPS—The nowcasting initiative. pySTEPS, accessed 17 May 2021, https://pysteps.readthedocs.io/en/latest/.

Reeves, H. D., and Y.-L. Lin, 2007: The effects of a mountain on the propagation of a preexisting convective system for blocked and unblocked flow regimes. *J. Atmos. Sci.*, **64**, 2401–2421, https://doi.org/10.1175/JAS3959.1.

Richard, E., S. Cosma, P. Tabary, J. Pinty, and M. Hagen, 2003: High-resolution numerical simulations of the convective system observed in the Lago Maggiore area on 17 September 1999 (MAP IOP 2a). *Quart. J. Roy. Meteor. Soc.*, **129**, 543–563, https://doi.org/10.1256/qj.02.50.

Rotunno, R., and J. B. Klemp, 1982: The influence of the shear-induced pressure gradient on thunderstorm motion. *Mon. Wea. Rev.*, **110**, 136–151, https://doi.org/10.1175/1520-0493(1982)110<0136:TIOTSI>2.0.CO;2.

——, and J. Klemp, 1985: On the rotation and propagation of simulated supercell thunderstorms. *J. Atmos. Sci.*, **42**, 271–292, https://doi.org/10.1175/1520-0469(1985)042<0271:OTRAPO>2.0.CO;2.

——, and R. Ferretti, 2003: Orographic effects on rainfall in MAP cases IOP 2b and IOP 8. *Quart. J. Roy. Meteor. Soc.*, **129**, 373–390, https://doi.org/10.1256/qj.02.20.

——, and R. A. Houze, 2007: Lessons on orographic precipitation from the Mesoscale Alpine Programme. *Quart. J. Roy. Meteor. Soc.*, **133**, 811–830, https://doi.org/10.1002/qj.67.

Scheffknecht, P., S. Serafin, and V. Grubišić, 2017: A long-lived supercell over mountainous terrain. *Quart. J. Roy. Meteor. Soc.*, **143**, 2973–2986, https://doi.org/10.1002/qj.3127.

Seity, Y., S. Soula, P. Tabary, and G. Scialom, 2003: The convective storm system during IOP 2a of MAP: Cloud-to-ground lightning flash production in relation to dynamics and microphysics. *Quart. J. Roy. Meteor. Soc.*, **129**, 523–542, https://doi.org/10.1256/qj.02.03.

Serafin, S., and Coauthors, 2020: *Multi-Scale Transport and Exchange Processes in the Atmosphere over Mountains.* 1st ed. Innsbruck University Press, 44 pp., https://doi.org/10.15203/99106-003-1.

Soderholm, B., B. Ronalds, and D. J. Kirshbaum, 2014: The evolution of convective storms initiated by an isolated mountain ridge. *Mon. Wea. Rev.*, **142**, 1430–1451, https://doi.org/10.1175/MWR-D-13-00280.1.

Sturmarchiv Schweiz, 2021: Sturmarchiv Schweiz—Tornados. Sturmarchiv Schweiz, accessed 15 May 2021, https://www.sturmarchiv.ch/index.php?title=Tornados.

swisstopo, 2005: DHM25/200m. swisstopo, accessed 3 May 2021, https://www.swisstopo.admin.ch/de/geodata/height/dhm25200.html.

Trefalt, S., and Coauthors, 2018: A severe hail storm in complex topography in Switzerland—Observations and processes. *Atmos. Res.*, **209**, 76–94, https://doi.org/10.1016/j.atmosres.2018.03.007.

van der Walt, S., and Coauthors, 2014: scikit-image: Image processing in Python. *PeerJ*, **2**, e453, https://doi.org/10.7717/peerj.453.

Wade, A. R., and M. D. Parker, 2021: Dynamics of simulated high-shear, low-CAPE supercells. *J. Atmos. Sci.*, **78**, 1389–1410, https://doi.org/10.1175/JAS-D-20-0117.1.

Ward, P. J., and Coauthors, 2020: Review article: Natural hazard risk assessments at the global scale. *Nat. Hazards Earth Syst. Sci.*, **20**, 1069–1096, https://doi.org/10.5194/nhess-20-1069-2020.

Weisman, M. L., and J. B. Klemp, 1982: The dependence of numerically simulated convective storms on vertical wind shear and buoyancy. *Mon. Wea. Rev.*, **110**, 504–520, https://doi.org/10.1175/1520-0493(1982)110<0504:TDONSC>2.0.CO;2.

Wu, F., and K. Lombardo, 2021: Precipitation enhancement in squall lines moving over mountainous coastal regions. *J. Atmos. Sci.*, **78**, 3089–3113, https://doi.org/10.1175/JAS-D-20-0222.1.

Zipser, E. J., D. J. Cecil, C. Liu, S. W. Nesbitt, and D. P. Yorty, 2006: Where are the most intense thunderstorms on Earth? *Bull. Amer. Meteor. Soc.*, **87**, 1057–1072, https://doi.org/10.1175/BAMS-87-8-1057.